Dalton Transactions

PAPER

View Article Online
View Journal | View Issue

Cite this: *Dalton Trans.*, 2025, **54**, 2908

A mononuclear iron(II) complex constructed using a complementary ligand pair exhibits intrinsic luminescence–spin-crossover coupling†

Du-Yong Chen,[a] Cheng Yi,[a] Xin-Feng Li,[a] Ren-He Zhou,[a] Li-Yan Zhang,[a] Rui Cai,[b] Yin-Shan Meng *[a,c] and Tao Liu *[a,c]

Received 13th November 2024,
Accepted 30th December 2024

DOI: 10.1039/d4dt03177f

rsc.li/dalton

Molecular materials that exhibit synergistic coupling between luminescence and spin-crossover (SCO) behaviors hold significant promise for applications in molecular sensors and memory devices. However, the rational design and underlying coupling mechanisms remain substantial challenges in this field. In this study, we utilized a luminescent complementary ligand pair as an intramolecular luminophore to construct a new Fe-based SCO complex, namely $[FeL_1L_2](BF_4)_2\cdot H_2O$ (**1-Fe**, L_1 is a 2,2′:6′,2′′-terpyridine (TPY) derivative ligand and L_2 is 2,6-di-1*H*-pyrazol-1-yl-4-pyridinecarboxylic acid), and two isomorphic analogs (**2-Co**, $[CoL_1L_2](BF_4)_2\cdot H_2O$ and **3-Zn**, $[ZnL_1L_2](BF_4)_2\cdot H_2O$). Magnetic studies reveal that **1-Fe** exhibits thermally induced SCO within the temperature range of 150–350 K. Variable-temperature fluorescence emission spectral analysis of the three complexes confirmed the occurrence of SCO–luminescence coupling in **1-Fe**. Furthermore, variable-temperature UV-vis absorption spectra and time-dependent density functional theory (TD-DFT) calculations elucidate the intramolecular luminescence emission behavior, highlighting the critical role of charge transfer processes between the L_1 ligand and Fe^{II} ions with different spin states. Our research presents a novel construction strategy for synthesizing synergistic SCO–luminescent materials and contributes to the understanding of the mechanisms underlying SCO–luminescence coupling.

Introduction

Spin-crossover (SCO) molecules are a class of $3d^4$–$3d^7$ transition metal complexes whose 3d electron configurations can be regulated by external stimuli such as light, heat, pressure, or changes in the chemical environment.[1–7] This regulation induces a spin-transition process, positioning SCO molecules as promising candidates for stimuli-responsive smart materials.[8–10] The intrinsic spin state transition directly influences the molecular magnetic moment. Additionally, alterations in the 3d electron configuration lead to variations in the local coordination geometry of metal ions, which, in turn, affect charge distribution and electric polarization properties.[11] These changes can sometimes even result in magnetodielectric and even magnetoelectric coupling,[12,13] rendering them as promising candidates in applications of SCO molecule-based sensing, switching and spintronic devices.

Regarding the luminescence properties of the SCO complex, the energy transfer process between the luminophore and the metal ion is contingent upon the spin state of the metal ion.[14] Consequently, spin transitions can induce variations in luminescence intensity, enabling the realization of SCO-regulated luminescence.[15] This phenomenon facilitates the monitoring of the spin state through luminescence signals, thereby presenting potential applications in spin-optic-based molecular memory devices. Over the past decade, numerous synthetic strategies have been developed to construct luminescence-coupled SCO molecular systems. These strategies range from the substitution of mononuclear complexes, and grafting on one-dimensional molecular chains, to the design of two- and three-dimensional luminescent Hofmann-type frameworks, as well as the integration with luminescent rare-earth complexes.[16–20] Among the molecular SCO systems, mononuclear ones are particularly attractive due to their concise structures and synthesis routes, clear structure–property relationships, and the wealth of existing research

---

[a] *State Key Laboratory of Fine Chemicals, Frontier Science Center for Smart Materials, School of Chemical Engineering, Dalian University of Technology, No. 2 Linggong Road, Dalian 116024, P. R. China.*
E-mail: mengys@dlut.edu.cn, liutao@dlut.edu.cn
[b] *Instrumental Analysis Center, Dalian University of Technology, No. 2 Linggong Road, Dalian 116024, P. R. China*
[c] *Liaoning Binhai Laboratory, Dalian 116023, P. R. China*

† Electronic supplementary information (ESI) available: Fluorescence spectra of the ddxc-abpt ligand and details of the complexes including TGA traces, X-ray single-crystal data and structures, PXRD patterns, fluorescence spectra, and theoretical calculation data. CCDC 2396863 (for **1-Fe** at 120 K), 2396864 (for **1-Fe** at 300 K), 2396865 (for **2-Co** at 300 K) and 2396866 (for **3-Zn** at 300 K). For ESI and crystallographic data in CIF or other electronic format see DOI: **https://doi.org/10.1039/d4dt03177f**

examples. The Fe^{II} SCO complex synthesized using tridentate-substituted pyridine-type ligands has emerged as the most extensively studied mononuclear complex. This type of ligand has many modification-accessible sites, thus enabling the integration of various luminescent groups.[21,22]

Recent studies have demonstrated a few examples of luminescence–SCO complexes, with the coupling mechanism predominantly attributed to Förster resonance energy transfer (FRET).[23] This theory posits that the overlap of the complexes' absorption spectra with the emission spectra of the luminophore is crucial for energy transfer between the metal ion and the luminophore, as well as the distance between them.[24]

Concerning the relative distance and degree of conjugation between the luminophore and the SCO center, the tethering modes of the luminophore to the SCO ligand can be categorized into intermolecular and intramolecular luminophores. Intermolecular luminophores exhibit larger spatial distances and low orbital hybridization with the metal ion, while intramolecular luminophores are characterized by smaller distances and higher orbital hybridization with the metal ion. In the case of intermolecular luminophores, the FRET mechanism remains predominant. However, a recent study revealed that for intramolecular luminophores, the 3d orbitals of the metal ion hybridize with the molecular orbitals of the luminophore, complicating the excitation and emission processes, which might not simply be attributed to FRET between the metal ion and the luminophore.[25] DFT calculations suggested that complex excitation and emission processes including a metal-to-ligand charge transfer (MLCT) process within the molecule were involved. Nonetheless, subsequent investigations on intramolecular luminescence cases are still scarce.

We are interested in the synergetic mechanism in luminescence–SCO molecules that are characterized by intramolecular luminophores. Recently, our group has constructed a series of mononuclear Fe^{II}-based SCO complexes by employing a complementary 2,2′:6′,2″-terpyridine (TPY)-derivative ligand.[26] The use of the complementary pair strategy offers several advantages, including improved solubility, crystallinity and the modification ability of the target SCO complexes.[27] As a consequence, it serves as an effective research platform for investigating luminescence–SCO coupling phenomena. In this work, we synthesized a new Fe^{II}-based SCO complex by employing a complementary 2,2′:6′,2″-terpyridine (TPY) derivative (L$_1$) and a 2,6-di-1*H*-pyrazol-1-yl-4-pyridinecarboxylic acid (L$_2$) ligand pair, $[FeL_1L_2](BF_4)_2\cdot H_2O$, characterized by an asymmetric coordination mode, in which the ligands act as an intramolecular luminophore. This complex exhibits a synergistic relationship between SCO and luminescence emission. As a comparison study, cobalt and zinc analogs were also synthesized and characterized. By combining experimental spectroscopy with DFT calculations, we found that the orbital contributions of the iron atom are non-negligible during excitation. The observed discrepancies in the luminescence intensity of this complex is strongly associated with the involved excited states, where the iron atomic orbitals play a critical role.

Experimental

Materials and synthesis

The ligand L$_2$ and all other chemicals are commercially available and were used without further purification. The L$_1$ ligand was synthesized according to the procedure described in the literature.[27] Complex $[ML_1L_2](BF_4)_2\cdot H_2O$ (M = Fe, Co, Zn) was synthesized by solvent evaporation at room temperature. The detailed synthesis method is described below. To the suspension of L$_1$ (0.0581 g, 0.1 mmol) and L$_2$ (0.0253 g, 0.1 mmol) in 10 mL of dichloromethane, $Fe(BF_4)_2\cdot 6H_2O$ (0.0337 g, 0.1 mmol) in 5 mL of methanol was added. The mixture turned clear after vigorously stirring it for 20 min, and the solution was filtered (Scheme 1). Bulky crystals (**1-Fe**) could be obtained by slow solvent evaporation at room temperature for 4–5 days (yield: 40%). The other complexes (**2-Co** and **3-Zn**) were synthesized *via* the same method as that for **1-Fe** but using different metal salts (49 mg, yield: 45% for **2-Co**; yield: 43% for **3-Zn**). Elemental analysis (%) for $C_{49}H_{42}N_8O_7B_2F_8Fe$ (**1-Fe**): C 54.27, H 3.90, N 10.33; found: C 54.54, H 4.07, N 10.08. Elemental analysis (%) for $C_{49}H_{42}N_8O_7B_2F_8Co$ (**2-Co**): C 54.12, H 3.89, N 10.30; found: C 54.35, H 3.94, N 10.16. Elemental analysis (%) for $C_{49}H_{42}N_8O_7B_2F_8Zn$ (**3-Zn**): C 53.80, H 3.87, N 10.24; found: C 54.13, H 3.98, N 10.02.

Physical measurements

Single-crystal XRD data collection and structure refinement. All single-crystal XRD data were collected using a Bruker D8 Venture CMOS-based diffractometer (Mo-Kα radiation, λ = 0.71073 Å) using SMART and SAINT programs. The final unit-cell parameters were based on all observed reflections from integration of all frame data. The structures were solved with the ShelXT structure solution program using intrinsic phasing by using Olex2-1.5. For all compounds, the final refinement was performed using full matrix least-squares methods with anisotropic thermal parameters for non-hydrogen atoms on F^2. Hydrogen atoms were added theoretically and riding on the atoms under consideration.

Thermogravimetric analysis (TGA). Thermogravimetric analysis (TGA) was performed using TG/DTA Q600 (Mettler Toledo) instruments under a nitrogen atmosphere at a warming rate of 10 K min^{-1} from ambient temperature to 600 K.

Powder X-ray diffraction (XRD). Powder X-ray diffraction (PXRD) data for solvated samples were collected on a Bruker

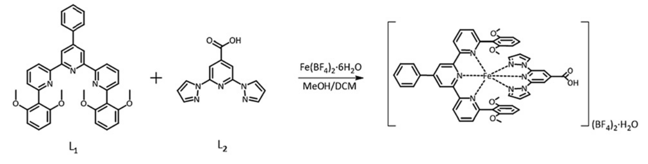

Scheme 1 Synthesis route and structures of the 2,2′:6′,2″-dimethoxyphenyl-substituted TPY ligand (L$_1$) and 2,6-di-1*H*-pyrazol-1-yl-4-pyridinecarboxylic acid (L$_2$).

D8 Venture diffractometer using a Cu Kα radiation source (λ = 1.54178 Å) in the range of 5° < 2θ < 50° at ambient temperature.

Magnetic measurements. Magnetic measurements of the samples were performed using a Quantum Design PPMS-9 instrument. Measurements were performed using finely ground microcrystalline powders restrained in parafilm with polycarbonate capsules. Data were corrected for the diamagnetic contribution calculated from Pascal constants and background from the parafilm and capsules.

UV-vis absorption spectroscopy. UV-vis absorption spectra of the solid samples were recorded using a HITACHI HU4150 spectrophotometer (HITACHI Company, Tokyo, Japan) and cooled by liquid nitrogen in a temperature range from 80 to 400 K.

Luminescence spectroscopy. The luminescence spectra of the solid samples were recorded using an Edinburgh FLS1000 fluorescence spectrophotometer (Edinburgh Company, Edinburgh, United Kingdom) equipped with a liquid-nitrogen-filled cryostat (Oxford).

Theoretical calculations. All calculations were performed using the Gaussian 16 program package at the PBE0 level.[28] The LANL2TZ pseudopotential basis set was used for the Fe atom,[29,30] and the 6-311g (d,p) Pople basis set was used for other atoms.[31] Energy calculation was based on the H-optimized crystalline geometries, and the keyword "stable = opt" was used to ensure the stability of the ground-state wavefunction. For the LS state (spin multiplicity = 1), the restricted determinant was used, whereas for the HS state (spin multiplicity = 5), the unrestricted determinant was introduced. The keyword "IOp(9/40 = 4)" was added to the TD-DFT calculation to output excitation orbital pairs with configuration coefficients of >0.0001 for hole–electron excitation analysis by Multiwfn. Additional keywords for saving NAOs were added. Absorption spectral simulation, hole/electron analysis, and NAO orbital composition analysis were performed with Multiwfn.[32,33]

Results and discussion

Crystallography

A dark red bulky crystal of $[FeL_1L_2](BF_4)_2 \cdot H_2O$ (dark brown bulky for **2-Co** and clear white for **3-Zn**) was obtained to determine the crystal structure *via* single-crystal X-ray diffraction (SC-XRD). SC-XRD data revealed that all complexes crystallize in the orthorhombic space group *Pbca* with Z = 8, displaying nearly identical structures at different temperatures (Fig. 1 for **1-Fe** and Fig. S4† for **2-Co** and **3-Zn**). The mononuclear complex adopts a staggered arrangement, where two tetrafluoroborate ions and a water molecule are stabilized by the hydrogen bond, forming a hydrogen-bonded chain from the carboxylic group of L_2 through a water molecule to the tetrafluoroborate ion located in the void. Varying coordination bond lengths of the FeN_6 coordination sphere are summarized in Table S4.† The average Fe–N bond length is 2.135 Å for **1-Fe** at 300 K, indicating a high-spin state Fe^{II} with S = 2. The SC-XRD experiment at 120 K for **1-Fe** shows an observable coordination geometry change around the Fe^{II} center compared with the structure at 300 K, while the crystal retains the same space group and packing modes. The average Fe–N bond length shortens from 2.135 Å to 1.981 Å and the geometry distortion degree of the Fe-coordination sphere, Σ, which is defined as the total deviation of the 12 *cis* N–Fe–N angles from 90°, changes from 134.46° to 92.17°. The deviation degree to the ideal octahedron calculated using the SHAPE 2.0 program also has the same tendency, showing the variation in the CShM value from 4.521 at 300 K to 2.235 at 120 K. These geometry changes clearly demonstrate the spin transition of Fe^{II}, which is consistent with previously reported SCO Fe^{II} complexes.[34,35] In contrast, for complex **1-Co**, both the Co–N bond lengths and geometry distortion show tiny changes from 300 to 120 K, indicating that Co is stabilized in the low spin state.

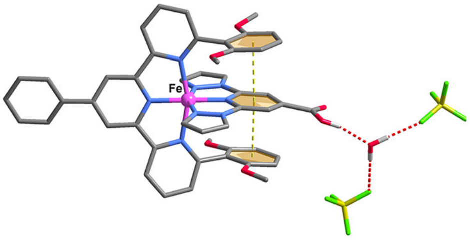

Fig. 1 Crystal structure of **1-Fe**.

Magnetic properties

To investigate the possible SCO behavior, temperature-dependent magnetic susceptibility measurements were performed (Fig. 2). For **1-Fe**, the $\chi_m T$ value at 100 K is only 0.17 cm^3 mol^{-1} K, revealing that **1-Fe** is in its LS state (S = 0). In the heating process, the $\chi_m T$ value began to increase from 0.36 cm^3 mol^{-1} K at 150 K to 3.5 cm^3 mol^{-1} K at 300 K, thus confirming the LS to HS transition. The spin transition nearly completed at around 350 K, showing a $\chi_m T$ value of 4 cm^3 mol^{-1} K, which is

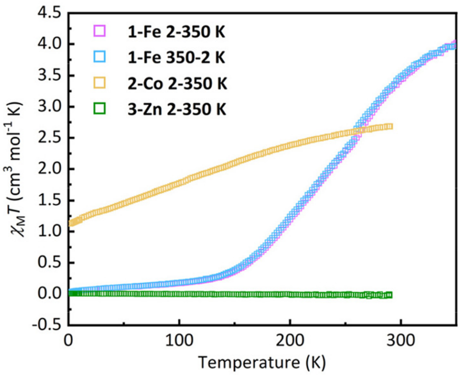

Fig. 2 Temperature dependence of the magnetic susceptibility for the **1-Fe**/**2-Co**/**3-Zn** complexes in the solid state.

higher than the spin-only value of HS Fe^{II}, but still within the typical range for mononuclear Fe^{II}-based SCO complexes.[36,37] Subsequent measurement in the cooling mode revealed no thermal hysteresis. Temperature-dependent magnetic susceptibility measurements were also performed on **2-Co** and **3-Zn** for comparison. For the **2-Co** complex, the $\chi_m T$ value shows a gradual increase over the entire measured temperature range, which can be ascribed as the stark sublevel depopulation caused by zero-field splitting.

Luminescence properties

To investigate the possible coupling between SCO and luminescence, temperature-dependent fluorescence spectra were recorded for complexes **1-Fe**, **2-Co**, **3-Zn** and the ligands in the solid state from 80 to 300 K. For ligand L_1, there are two emission bands: a broad band centred at 525 nm and two sharp peaks located at around 400 nm. All these emission bands exhibit normal thermal quenching behaviour (Fig. S4†). For ligand L_2, a broad emission band is exhibited with three maxima between 420 and 500 nm upon excitation at 365 nm across the temperature range of 80 to 300 K. The strongest peak appears at 438 nm with two shoulders at 420 and 460 nm. Interestingly, the luminescence intensity of L_2 shows a slight enhancement upon heating (Fig. S5†). For **2-Co**, the optimal excitation wavelength is 365 nm. The emission spectrum becomes significantly broader and contains three peaks located at 439 nm, 466 nm and 508 nm. The luminescence intensity of **2-Co** gradually decreased upon heating to room temperature, which is characteristic of a typical thermal quenching of luminescence (Fig. 3b). For **3-Zn**, strong luminescence emission is shown with a broad emission peak at 489 nm and a shoulder at 526 nm upon excitation at 396 nm (Fig. 3c). Both **2-Co** and **3-Zn** showed no abnormal enhancement of luminescence. For **1-Fe**, a similar emission band shape is shared with **2-Co** but it exhibits different luminescent behaviour (Fig. 3a). Fig. 3d shows the temperature-dependent luminescence emission intensities at 438 nm and the $\chi_m T$ values for **1-Fe** from 80 to 300 K. In the temperature range of 80–150 K, the luminescence intensity gradually decreased due to the thermal quenching effect. After that, the emission intensity remains at a nearly constant value until 225 K. Further increasing the temperature leads to a rapid increase in emission intensity. Although the abnormal increase in luminescence intensity of the **1-Fe** complex upon heating resembles that of ligand L_2, it is important to note that both the complexes **2-Co** and **3-Zn** exhibit the thermal quenching effect of luminescence, while **1-Fe** undergoes SCO. A dramatic increase in luminescence intensity is observed at temperatures between 225 and 300 K, which is also the temperature range of the SCO. This suggests strong coupling between them.

The strong coupling between SCO and luminescence in this simple mononuclear complex is uncommon, which encourages us to further investigate the coupling mechanism. First, variable-temperature solid-state UV-vis absorption spectra of **1-Fe** were recorded from 80 to 300 K. As shown in Fig. 4a, **1-Fe** exhibits a slight absorption difference at around 360 nm between 80 K and 300 K. The broad band from 300 nm to 800 nm can be attributed to MLCT and the d–d transition of Fe^{II}.[38,39] Furthermore, changes in the absorption intensity and wavelength at 700 nm and 1200 nm can be attributed to the spin transition of Fe^{II}, which is consistent with prior studies.[40] Energy calculations using density functional theory (DFT) and time-dependent density functional theory (TD-DFT) calculations were also conducted on LS and HS to acquire deeper insight into the charge and energy transfer processes. The calculated results were analyzed using the Multiwfn program.[32,33] As shown in Fig. S6,† nearly all the spin density is localized on the Fe atom for HS. According to

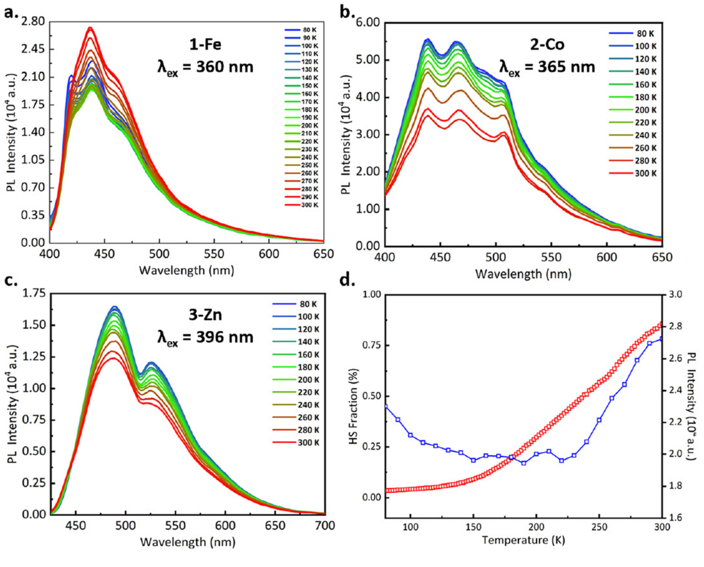

Fig. 3 Temperature-dependent luminescence emission spectra of the **1-FeII/2-CoII/3-ZnII** complexes (a–c) in the solid state. (d) Plots of the HS fraction of Fe^{II} (red squares) and luminescence emission intensity at 438 nm (blue squares) as a function of temperature for the **1-Fe** complex.

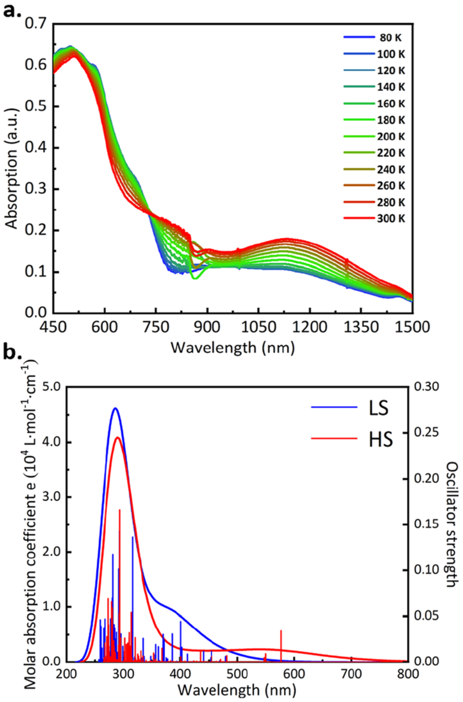

Fig. 4 (a) Temperature-dependent UV-vis absorption spectra of **1-Fe** in the solid state in the wavelength range from 450 to 1500 nm. (b) TD-DFT-calculated UV-vis spectra of Fe^{II} complexes in the LS and HS states.

Mulliken population analysis based on energy calculations, the spin population is 3.818, close to the value of 4 predicted by classic ligand field theory (Table S7†).[41,42] TD-DFT calculations were conducted to estimate the transition energies and features of vertical transitions. To ensure the calculated absorption wavelengths cover the visible spectral region, 252 lowest excited states for LS and 452 lowest excited states for HS were computed. The simulated absorption spectra for the HS and LS states were obtained under vacuum conditions (Fig. 4b), with transitions exhibiting oscillator strengths greater than 0.005; their components are listed in Tables S8–10†. Both LS and HS exhibit numerous excited states in the range of 200–400 nm. The excited state with the largest oscillator strength (excited state 163 for LS and excited state 320 for HS, Fig. 5) appears at 293 nm, with the scheme and orbital transition contributions shown in Fig. 5c and d.

From the calculated absorption spectrum, the main absorption peaks of both the LS and HS complexes lie in range of 250–350 nm, with HS showing lower absorption around the main peak compared with LS. Additionally, LS displays a shoulder peak at 400 nm, while HS has a broad satellite peak at around 575 nm. These features of calculated UV spectra resemble those of the experimental UV-vis spectrum, indicating that the TD-DFT calculation is reliable for qualitative analysis of electron transitions. To further understand the excitation behaviour, hole–electron analysis was conducted on excited states with oscillator strengths larger than 0.1, and differences in the molecular orbitals involved in the main

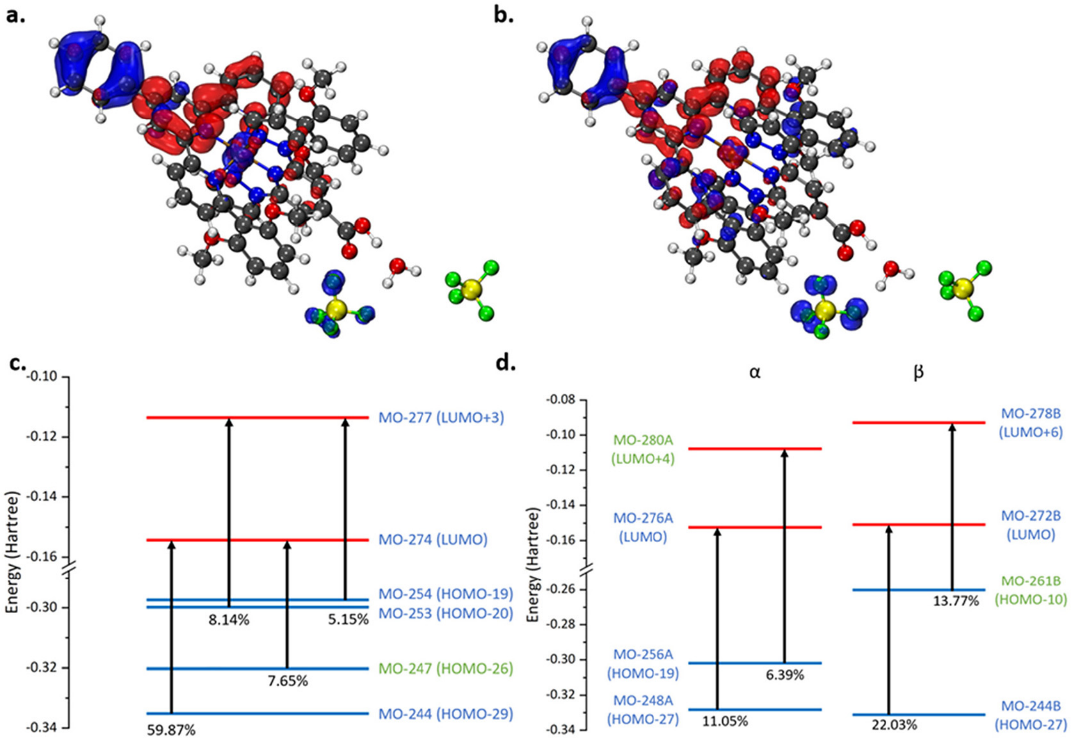

Fig. 5 Hole (blue)–electron (red) distribution caused by excited LS state 163 (a) and excited HS state 320 (b) for Fe^{II} complexes. Scheme and orbital transition contributions of excited state 163 for LS (c) and excited state 320 for HS (d) (blue-labelled MO values contain the contribution of Fe 3d NAOs).

Table 1 Composition of the Fe NAOs under excitation correlated with the MOs

	Fe atom contribution				Type of NAOs	
MO	Core (%)	Valence (%)	Rydberg (%)	Total (%)	Label	Composition (%)
Low spin state						
244	0.006	10.549	0.002	10.558	d_{xy}	10.005
253	0.004	55.123	0.051	55.178	d_{xy}	11.136
					d_{xz}	0.642
					d_{yz}	40.845
					$d_{x^2y^2}$	2.214
254	0.005	38.301	0.027	38.333	d_{xy}	11.909
					d_{xz}	4.884
					d_{yz}	20.766
					$d_{x^2y^2}$	0.676
274	0.002	3.276	0.010	3.288	d_{xz}	2.699
277	0.000	1.439	0.017	1.457	d_{yz}	1.197
High spin state						
248A	0.000	3.486	0.001	3.487	d_{xz}	3.294
256A	0.003	3.279	0.015	3.297	$d_{x^2y^2}$	1.732
					d_{z^2}	1.284
276A	0.003	1.365	0.01	1.377	p_z	0.638
					d_{xz}	0.677
244B	0.003	2.785	0.006	2.794	d_{xz}	2.566
272B	0.005	10.031	0.074	10.110	d_{xy}	4.178
					d_{xz}	2.772
					d_{yz}	1.814
					$d_{x^2y^2}$	0.757
278B	0.000	5.303	0.168	5.471	d_{xy}	2.934
					d_{yz}	1.817

excited state of HS and LS were clarified through atomic orbital component analysis (NAO analysis).[41] According to the hole–electron analysis for LS, the main excited state 163 involves electron transition within L_1 from the substituted benzene to the TPY ligand and a d–d transition of Fe. The HS molecule shows a similar distribution of electron and hole patterns on the ligand but with smaller contributions from Fe. Furthermore, Mulliken population analysis was used to estimate atom contributions to the holes and electrons. As shown in Tables S12 and S13,† Fe has a significant contribution to both LS and HS excited states, with 15.08% of the electron composition and 3.92% of the hole composition derived from Fe in LS. The integration of electron density difference on the Fe atom is negative, indicating metal to ligand electron transfer. For HS, 3.71% of the electron composition and 7.05% of the hole composition are contributed by Fe. The positive difference value indicates an inverse charge transfer from the ligand to Fe. NAO analysis was further conducted to characterize the contribution of the Fe atom in molecular orbitals involved in excited state 163 (Table 1). For the LS state, the analysis shows that Fe atom orbitals make a significant contribution to most transition-related orbitals except for MO-247, which is dominated by counter ions and solvents. The Fe atom 3d orbitals are largely involved in the occupied orbital, while the unoccupied orbital is primarily dominated by the TPY ligand. For the HS state, the contribution of the Fe atom orbitals in the occupied orbital is significantly reduced, but they appear to contribute more hybridization of the LUMO and a series of unoccupied low energy β spin orbitals, inducing an LMCT process upon light irradiation. Hole–electron analysis was also conducted on other excited states with oscillator strengths larger than 0.1 (Fig. S7†). These excited states did not match any excited state in HS with oscillator strengths larger than 0.05 (excited states with lower oscillator strengths can be considered forbidden transitions), and the metal ion also has a notable composition in these excited states. In contrast, there is only one excited state in HS with oscillator strengths larger than 0.1 (excited state 320 with an oscillator strength of 0.1662), and the excited state composition of the metal ion is much lower than LS. These observations indicated two distinct electron transition processes in LS and HS, and the non-negligible charge transfer between the ligand and Fe is partially reversed (metal to ligand for LS but ligand to metal for HS), which may lead to the observed anomalous luminescence variation. Furthermore, fewer excited states in HS also lead to reduced self-absorption, which could also lead to luminescence enhancement.

Conclusions

In summary, we synthesized the **1-Fe** complex using a complementary ligand pair, which can be characterized as an intramolecular luminophore. The temperature-dependent luminescence studies, in comparison with **2-Co**, **3-Zn** and the free ligands, reveal the SCO-regulated luminescence of **1-Fe**. Detailed density functional theory (DFT) calculations provide additional information for the coupling mechanism. Electron–hole analysis suggests the photoinduced charge transfer between the Fe atom and the TPY ligand, while NAO analysis indicates hybridization between the Fe 3d orbital and the molecular orbitals of the TPY ligand, consistent with the intramolecular luminophore mechanism. Notably, the Fe atom shows a reduced composition in both the excited states and molecular orbitals for the HS state. The largest oscillator strength for the excited state in the HS state is greater than in the LS state but has a lower absorption coefficient, indicating reduced self-absorption during the emission process. We hope that this approach will inspire development of SCO-regulated luminescent materials and devices.

Data availability

The data supporting this study's findings are available from the corresponding author upon request.

The data supporting this article have been included as part of the ESI† and can be obtained freely by asking the authors.

Conflicts of interest

There are no conflicts to declare.

Acknowledgements

This work was supported by the National Natural Science Foundation of China (Grants 22222103, 22025101, and 22173015), the Fundamental Research Funds for the Central Universities (DUT22LAB606), and the Liaoning Binhai Laboratory (Grant LBLE-2023-02), China.

References

1 Z.-z. Gu. Shinya Hayami and H. Yoshiki, *J. Am. Chem. Soc.*, 2001, **123**, 11644–11650.
2 A. E. A. Robert, J. Deeth and M. J. Wilcockson, *J. Am. Chem. Soc.*, 2010, **132**, 6876–6877.
3 S. Brooker, *Chem. Soc. Rev.*, 2015, **44**, 2880–2892.
4 M. G. Cowan, J. Olguin, S. Narayanaswamy, J. L. Tallon and S. Brooker, *J. Am. Chem. Soc.*, 2012, **134**, 2892–2894.
5 M. A. Halcrow, *Chem. Soc. Rev.*, 2011, **40**, 4119–4142.
6 S. Ohkoshi, K. Imoto, Y. Tsunobuchi, S. Takano and H. Tokoro, *Nat. Chem.*, 2011, **3**, 564–569.
7 J. A. Real, A. B. Gaspar and M. C. Munoz, *Dalton Trans.*, 2005, 2062–2079.
8 A. Enriquez-Cabrera, A. Rapakousiou, M. Piedrahita-Bello, G. Molnár, L. Salmon and A. Bousseksou, *Coord. Chem. Rev.*, 2020, **419**, 213396.
9 M. D. Manrique-Juárez, F. Mathieu, A. Laborde, S. Rat, V. Shalabaeva, P. Demont, O. Thomas, L. Salmon, T. Leichle, L. Nicu, G. Molnár and A. Bousseksou, *Adv. Funct. Mater.*, 2018, **28**, 1801970.
10 G. Molnár, S. Rat, L. Salmon, W. Nicolazzi and A. Bousseksou, *Adv. Mater.*, 2018, **30**, 1703862.
11 N. T. Yao, L. Zhao, H. Y. Sun, C. Yi, Y. H. Guan, Y. M. Li, H. Oshio, Y. S. Meng and T. Liu, *Angew. Chem., Int. Ed.*, 2022, **61**, e202208208.
12 V. B. Jakobsen, S. Chikara, J. X. Yu, E. Dobbelaar, C. T. Kelly, X. Ding, F. Weickert, E. Trzop, E. Collet, H. P. Cheng, G. G. Morgan and V. S. Zapf, *Inorg. Chem.*, 2021, **60**, 6167–6175.
13 M. Owczarek, M. Lee, S. Liu, E. R. Blake, C. S. Taylor, G. A. Newman, J. C. Eckert, J. H. Leal, T. A. Semelsberger, H. P. Cheng, W. Nie and V. S. Zapf, *Angew. Chem., Int. Ed.*, 2022, **61**, e202214335.
14 J. Y. Ge, Z. Chen, L. Zhang, X. Liang, J. Su, M. Kurmoo and J. L. Zuo, *Angew. Chem., Int. Ed.*, 2019, **58**, 8789–8793.
15 C. F. Wang, R. F. Li, X. Y. Chen, R. J. Wei, L. S. Zheng and J. Tao, *Angew. Chem., Int. Ed.*, 2015, **54**, 1574–1577.
16 N. Deorukhkar, C. Egger, A. Rosspeintner and C. Piguet, *J. Am. Chem. Soc.*, 2024, **146**, 19386–19396.
17 M. Meneses-Sánchez, L. Piñeiro-López, T. Delgado, C. Bartual-Murgui, M. C. Muñoz, P. Chakraborty and J. A. Real, *J. Mater. Chem. C*, 2020, **8**, 1623–1633.
18 C. F. Wang, G. Y. Yang, Z. S. Yao and J. Tao, *Chem. – Eur. J.*, 2018, **24**, 3218–3224.
19 J. L. Wang, Q. Liu, Y. S. Meng, X. Liu, H. Zheng, Q. Shi, C. Y. Duan and T. Liu, *Chem. Sci.*, 2018, **9**, 2892–2897.
20 X.-R. Wu, S.-Q. Wu, Z.-K. Liu, M.-X. Chen, J. Tao, O. Sato and H.-Z. Kou, *Sci. China: Chem.*, 2024, **67**, 3339–3346.
21 M. A. Halcrow, *Coord. Chem. Rev.*, 2009, **253**, 2493–2514.
22 L. J. Kershaw Cook, R. Mohammed, G. Sherborne, T. D. Roberts, S. Alvarez and M. A. Halcrow, *Coord. Chem. Rev.*, 2015, **289–290**, 2–12.
23 C. Yi, Y.-S. Meng, L. Zhao, N.-T. Yao, Q. Liu, W. Wen, R.-X. Li, Y.-Y. Zhu, H. Oshio and T. Liu, *CCS Chem.*, 2023, **5**, 915–924.
24 L. Wu, C. Huang, B. P. Emery, A. C. Sedgwick, S. D. Bull, X. P. He, H. Tian, J. Yoon, J. L. Sessler and T. D. James, *Chem. Soc. Rev.*, 2020, **49**, 5110–5139.
25 Y. Jiao, J. Zhu, Y. Guo, W. He and Z. Guo, *J. Mater. Chem. C*, 2017, **5**, 5214–5222.
26 S. Y. Wang, J. H. Fu, Y. P. Liang, Y. J. He, Y. S. Chen and Y. T. Chan, *J. Am. Chem. Soc.*, 2016, **138**, 3651–3654.
27 S. Y. Zhang, H. Y. Sun, R. G. Wang, Y. S. Meng, T. Liu and Y. Y. Zhu, *Dalton Trans.*, 2022, **51**, 9888–9893.
28 C. Adamo and V. Barone, *J. Chem. Phys.*, 1999, **110**, 6158–6170.
29 P. J. Hay and W. R. Wadt, *J. Chem. Phys.*, 1985, **82**, 299–310.
30 B. P. Pritchard, D. Altarawy, B. Didier, T. D. Gibson and T. L. Windus, *J. Chem. Inf. Model.*, 2019, **59**, 4814–4820.
31 R. Krishnan, J. S. Binkley, R. Seeger and J. A. Pople, *J. Chem. Phys.*, 1980, **72**, 650–654.
32 T. Lu, *J. Chem. Phys.*, 2024, **161**, 082503.
33 T. Lu and F. Chen, *J. Comput. Chem.*, 2012, **33**, 580–592.
34 R. W. Hogue, H. L. Feltham, R. G. Miller and S. Brooker, *Inorg. Chem.*, 2016, **55**, 4152–4165.
35 J. L. Wang, Q. Liu, Y. S. Meng, H. Zheng, H. L. Zhu, Q. Shi and T. Liu, *Inorg. Chem.*, 2017, **56**, 10674–10680.

36 S. Chorazy, R. Podgajny, K. Nakabayashi, J. Stanek, M. Rams, B. Sieklucka and S. Ohkoshi, *Angew. Chem., Int. Ed.*, 2015, **54**, 5093–5097.

37 S. Kawabata, S. Chorazy, J. J. Zakrzewski, K. Imoto, T. Fujimoto, K. Nakabayashi, J. Stanek, B. Sieklucka and S. I. Ohkoshi, *Inorg. Chem.*, 2019, **58**, 6052–6063.

38 S. Zerdane, L. Wilbraham, M. Cammarata, O. Iasco, E. Riviere, M. L. Boillot, I. Ciofini and E. Collet, *Chem. Sci.*, 2017, **8**, 4978–4986.

39 W. Zhang, K. S. Kjaer, R. Alonso-Mori, U. Bergmann, M. Chollet, L. A. Fredin, R. G. Hadt, R. W. Hartsock, T. Harlang, T. Kroll, K. Kubicek, H. T. Lemke, H. W. Liang, Y. Liu, M. M. Nielsen, P. Persson, J. S. Robinson, E. I. Solomon, Z. Sun, D. Sokaras, T. B. van Driel, T. C. Weng, D. Zhu, K. Warnmark, V. Sundstrom and K. J. Gaffney, *Chem. Sci.*, 2017, **8**, 515–523.

40 A. Marino, P. Chakraborty, M. Servol, M. Lorenc, E. Collet and A. Hauser, *Angew. Chem., Int. Ed.*, 2014, **53**, 3863–3867.

41 Z. Liu, T. Lu and Q. Chen, *Carbon*, 2020, **165**, 461–467.

42 L. U. Tian and C. Fei-Wu, *Acta Phys. – Chim. Sin.*, 2012, **28**, 1–18.